Rail vehicle dynamic response to the nonlinear physical in-service model of its secondary suspension hydraulic dampers

W.L. Wang[a, b*], D.S. Yu[c], Q.H. Qin[b], S. Iwnicki[d]

[a] *School of Mechanical Engineering, Dongguan University of Technology, Dongguan 523808, P. R. of China*

[b] *State Key Laboratory for Strength and Vibration of Mechanical Structures, Xi'an Jiaotong University, Xi'an 710049, P. R. of China*

[c] *Anhui Xingrui Gear Transmission Co., Ltd, Lu'an 237161, P. R. of China*

[d] *Institute of Railway Research, University of Huddersfield, Huddersfield HD1 3DH, UK*

Abstract

A full nonlinear physical in-service model was built for a rail vehicle secondary suspension hydraulic damper with shim-pack-type valves. In the modelling process, a shim pack deflection theory with an equivalent-pressure correction factor was proposed and the Finite Element Analysis (FEA) approach was assisted. Followed bench test results validated the damper model over its full velocity range, and thus also proved the proposed shim pack deflection theory and the FEA-based parameter identification approach are effective. The validated full damper model was then incorporated into a detailed vehicle dynamics simulation to study how its key in-service parameter variations influence the secondary suspension related vehicle system dynamics. The obtained nonlinear physical in-service damper model and the vehicle dynamic response characteristics in this study could be used in product design optimisation and nonlinear optimal specification of high-speed rail hydraulic dampers.

Keywords: Nonlinear modelling; hydraulic damper; shim pack deflection; FEA; in-service parameter; rail vehicle secondary suspension; ride comfort; curve negotiation stability

1. Introduction

The secondary suspension of a passenger rail vehicle usually employs both vertical and several lateral hydraulic dampers, which play important roles in the carbody vibration reduction, ride comfort improvement and curve negotiation stabilization. For hydraulic dampers are in practice very nonlinear devices (see Mellado et al. [1] and Wang et al. [2]), with characteristics which are sensitive to the in-service conditions and could have unpredictable and significant influences on the vehicle system dynamics (see Wang et al. [3]), as speeds and loads increase in modern rail vehicles, these effects become more significant, so it is important to include exact representation of damper parameters for vehicle system dynamics study.

In related works, Kasteel et al. [4] and Farjoud et al. [5] built detailed nonlinear physical models for hydraulic dampers with shim stacks and orifices. Simms et al. [6] and Calvo et al. [7] performed simulations on the effects of damper characteristics on road vehicle dynamics, the macro damper models used include which has symmetric or asymmetric performance, which has simple linear or piecewise linear or linear with hysteresis performance; Park et al. [8] carried out sensitivity analysis of suspension parameters on high-speed train

* Corresponding author at: School of Mechanical Engineering, Dongguan University of Technology, Dongguan 523808, Guangdong Province, PR China. Tel.: +86 769 22861122.

E-mail address: pianowwl@163.com (W.L. Wang).

Nomenclature

A_a	pressure acting area on a shim or shim pack (m^2)
B_1~B_5	constant coefficients
C	damping coefficient (N s/m)
C_{d1}, C_{d2}	discharge coefficients
C_e	equivalent-pressure correction factor
C_w	deflection coefficient of a shim or shim pack (m^6/N)
C_1~C_5	constant coefficients
E	elastic modulus (Pa)
F, F_b, F_r	damping force, bending force, damper saturation force (N)
K_e, K_{rubber}, K_w	effective stiffness, rubber attachment stiffness, bending stiffness (N/m)
M_b	bending torque (Nm)
P, P_b, P_e	working pressure, reservoir back pressure, equivalent pressure (Pa)
Q_{valve}	flow through the valve system (m^3/s)
R (m)	railway curve radius (m)
RMS_A_y	root mean square centrifugal acceleration of the carbody (m/s^2)
RMS_D_c	root mean square derailment coefficient
RMS_F_y	root mean square wheelset-rail lateral shift force (N)
RMS_W_n	root mean square total wear number (N)
T	oil temperature (℃)
V, V_r	vehicle speed (km/h), damper saturation speed (m/s)
W_{zy}, W_{zz}	lateral and vertical ride index
d_c	diameter of the constant orifice (m)
h, h_e,	shim thickness, equivalent thickness of a shim pack (m)
p_1~p_n	pressures acting on the shims of a shim pack (Pa)
r, r_n, r_w	radius, clamping radius and free radius of a shim (m)
s	damper displacement (m)
t	time (s)
v	damper velocity (m/s)
$w(r)$	disk deflection in terms of the radius (m)
$x_r(t)$	actual instantaneous displacement of the damper (m)
$2a$	small clearance between a damper and its two fixing seats (m)
ε_0	entrained air ratio of oil (%)
ν	poisson's ratio
ρ	instantaneous density of oil (kg/m^3)

dynamics, using commercial Multibody System (MBS) dynamics simulation software Vampire and Design of Experiments (DoE) approach, however, the hydraulic damper model used is a simple linear model which contains only one parameter, i.e., the damping coefficient.

In rail vehicle design studies, Shieh et al. [9] and He et al. [10] also used the simple linear hydraulic damper model for suspension optimization; Hao et al. [11], however, used the linear Maxwell damper model, i.e., a linear damping coefficient in series with a linear stiffness (see [12]), in the multi-objective optimization search, and obtained better results; Wang et al. [13] proposed a full nonlinear damper model concept which includes most of the in-service parameters and a detailed physical model was built, the nonlinear in-service damper model was then successfully used for the optimal specification of a locomotive axle-box hydraulic damper for vibration reduction and track-friendliness (see Wang et al. [14]).

For the research of how actual in-service parameters of the secondary suspension hydraulic dampers affect high-speed rail vehicle system dynamics is not adequate, in this work, a detailed nonlinear physical in-service model was built for a secondary suspension vertical hydraulic damper with shim-pack-type valves, in the modelling process, a shim pack deflection theory with an equivalent-pressure correction factor was proposed and the Finite Element Analysis (FEA) approach was assisted in the parameter identification; Followed comparison of simulation and test results prove that the established damper model captured the nonlinear damping characteristics over its full velocity range. The validated full damper model was then used for a detailed MBS simulation of a locomotive dynamic response to the in-service parameter variations of its secondary suspension hydraulic dampers. The obtained nonlinear in-service damper model and vehicle dynamic response could be instructive in product design optimization and optimal specification of modern rail vehicle hydraulic dampers.

2. Nonlinear physical in-service damper model

2.1. Physical mechanism

Figure 1 illustrates the structural configuration and working principle of a twin-tube hydraulic damper which is vertically used in a locomotive secondary suspension. The hydraulic damper employs shim-pack-type valves, which differ from the valves introduced in literatures [2] and [13], to produce fluid resistances and therefore damping forces.

When the damper is extended (Fig. 1b), the hydraulic oil in the rod-side chamber is forced through the piston feed passages and presses on the shim pack of the piston extension valve, when the shim pack is deflected, the hydraulic oil is discharged to the non-rod chamber with a certain resistance, then a relevant pressure P is produced in the rod-side chamber and a relevant extension damping force is produced and output by the rod, the faster the damper is extended, the higher pressure P and extension damping force will be produced; At the same time, to compensate volume expansion of the non-rod chamber, the hydraulic oil in the reservoir is sucked into the non-rod chamber through the check valve unit in the foot valve assembly, with a very low resistance. Additionally, the constant orifice in the piston is always free for the extension flow, but the piston compression valve and the compression valve unit in the foot valve assembly are closed by the extension flow.

When the damper is compressed (Fig. 1c), however, the hydraulic oil in the non-rod chamber can be both discharged to the rod-side chamber by deflecting the shim pack of the piston compression valve, and to the reservoir by deflecting that of the compression valve unit in the foot valve assembly. With a certain compressing speed, a relevant pressure P is produced in the non-rod chamber and a relevant compression damping force is produced and output by the rod. Similarly, the constant orifice is also free for the compression flow, but the piston extension valve and check valve unit in the foot valve assembly remain closed by the pressing action of the extension flow.

Figure 2 is a more detailed illustration of the piston assembly configuration and operating principle of the

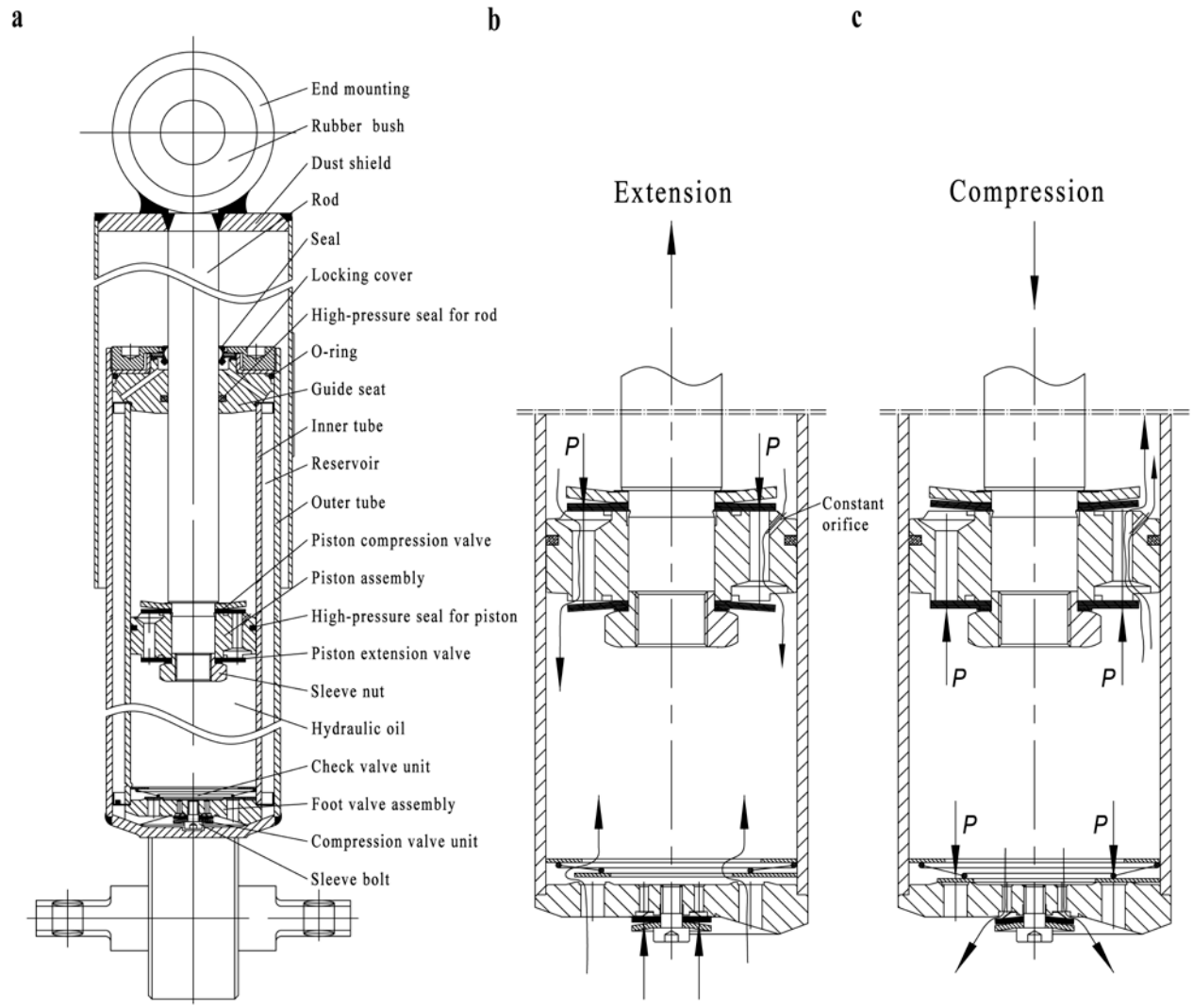

Fig. 1. Cross-section of a locomotive secondary suspension vertical hydraulic damper (a), working principle of the damper during its extension stroke (b) and its compression stroke (c).

piston valves. Fig. 2a shows that the piston compression valve uses four pieces of No. 1 shim and four pieces of No. 2 shim in its shim pack, and employs the first piece of No. 2 shim as the sealing shim; the piston extension valve, however, uses three pieces of No. 2 shim and four pieces of No. 3 shim in its shim pack, and also employs its first piece of No. 2 shim as the sealing shim; The three kinds of shims have uniform inner and outer radii, but different thicknesses.

A 6/6-hole piston has six holes as feed passages for the compression flow up into the raised six sealing bosses, and other six holes, from the lower area below boss level, as feed passages for the downward extension flow. The 6/6 holes separate with each other and uniformly distribute along the circumference; An inclined constant orifice is bored from a boss side to a feed passage to allow free leak from both directions.

Figures 2b and c combine to illustrate that the total pressure acting area on the shim pack surface of the

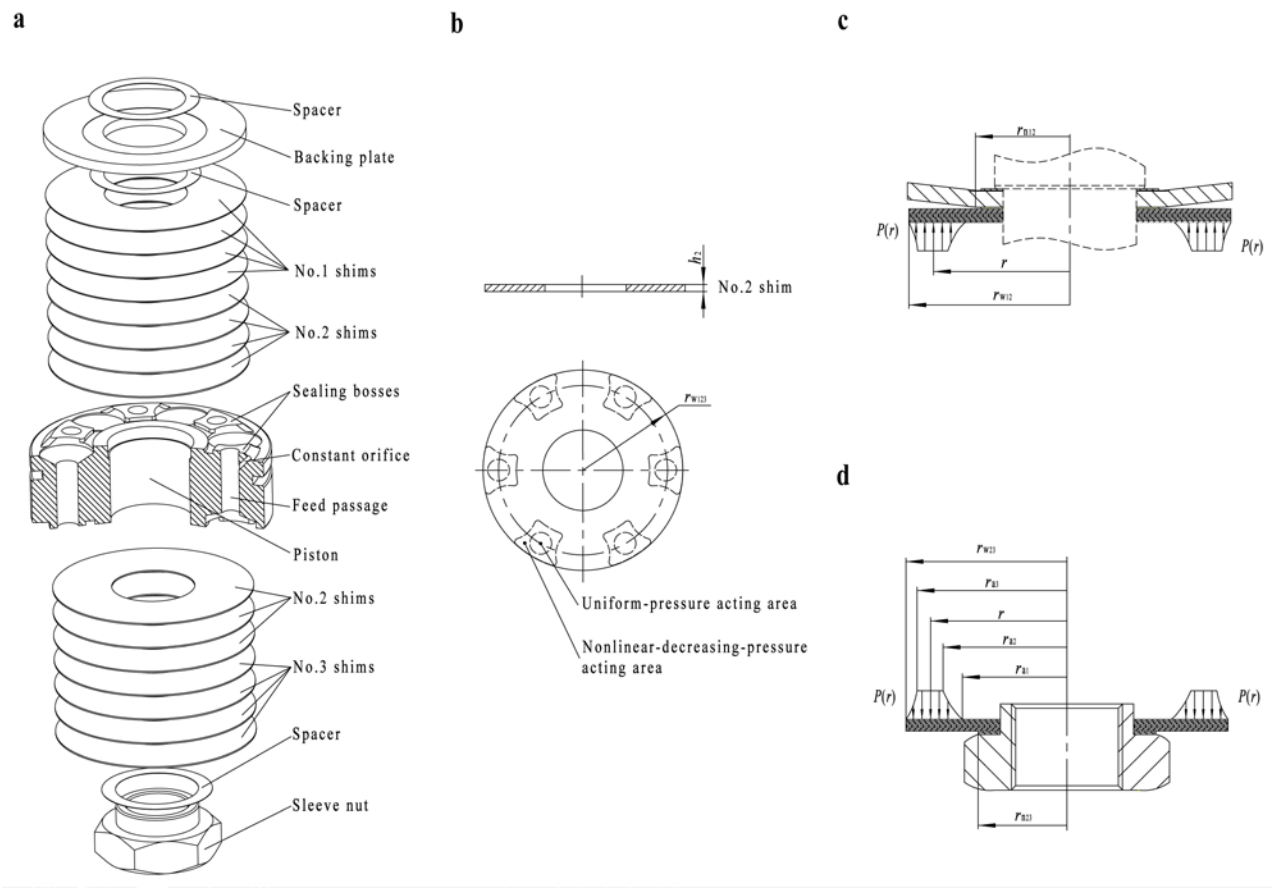

Fig. 2. Exploded view of the piston assembly (a), cross-section and schematic pressure acting areas on the surface of the sealing shim (No. 2 shim) (b), operating principle of the piston compression valve (c) and that of the piston extension valve (d).

piston compression valve, is the sum of the six projected areas of the six bosses on the sealing shim; In each projected area, the central circular is a uniform-pressure acting area, and the irregular area outside the circle is a nonlinear-decreasing-pressure acting area with zero marginal pressure. Fig. 2c shows that the shim pack will be deflected against the rigid backing plate by the pressing action of the compression flow, and therefore discharge the compression flow.

Operating principle of the piston extension valve (Fig. 2d) is similar to that of the piston compression valve, the extension flow acting area and pressure distribution law on the shim pack, are the same as that of the compression flow on the shim pack of the piston compression valve.

Similarly, Fig. 3 illustrates the configuration and operating principle of the foot valve assembly. In Fig. 3a, above the foot valve body, it's actually a check valve unit with a triangulated sealing shim and a weak flat spiral spring held by a retaining washer. When the damper extends, the reservoir oil is sucked into the non-rod chamber through the six extension feed passages, because stiffness of the flat spiral spring is pretty small and diameters of the six extension feed passages are large enough, opening resistance of the check valve usually could be neglected in engineering.

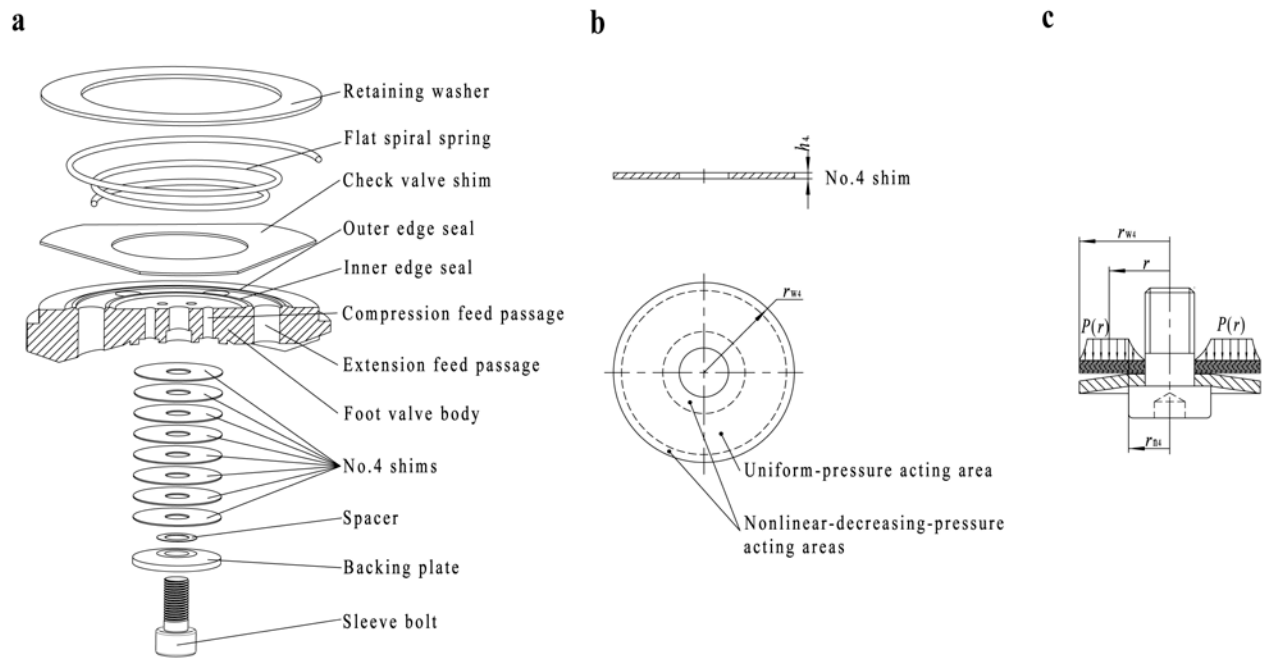

Fig. 3. Exploded view of the foot valve assembly (a), cross-section and schematic pressure acting areas on the surface of the sealing shim (No. 4 shim) (b) and operating principle of the compression valve unit in the foot valve assembly (c).

When the damper is compressed, however, the compression flow closes the check valve first, thus, it can only be forced through the central perforation of the check valve shim and into the six small compression feed passages inside the inner edge seal, and press on the shim pack of the compression valve unit below the foot valve body. As shown in Fig. 3a, the compression valve unit uses eight pieces of No. 4 shim in its shim pack, and employs the first piece of No. 4 shim as the sealing shim.

Figures 3b and c combine to illustrate that there are three annulus areas on the surface of the sealing shim. the middle larger annulus area is subjected to a continuous and uniform pressure, and the other two smaller annulus areas are both subjected to continuous but nonlinear-decreasing pressures with zero marginal values. Fig. 3c shows that the shim pack will be deflected against the rigid backing plate by the compression flow, and therefore discharge the compression flow.

2.2. Nonlinear modelling

2.2.1 Modelling scheme

This study borrows the nonlinear in-service damper model concept proposed in literature [13]. The proposed nonlinear in-service damper model, which includes a nonlinear hydraulic damping element, a tandem stiffness of oil, rubber bushes and fixing seats, and a small clearance element, is more detailed than the Maxwell [12] damper model and proved to be more suitable for modern high-speed transit problems.

The approaches for modelling the damper motions and forces, the variable oil properties and the flow losses of the secondary suspension vertical hydraulic damper, are similar to that introduced in [13]; For the valve

system configuration and operating mechanism are very different from that in previous papers, the valve system dynamics has to be solved in specialty.

Figures 2b, c and d show that the pressure acting areas on the piston valve shim packs are discrete. In each discrete acting area, the area outside the central circle is irregular, and the nonlinear-decreasing-pressure law acting on it is hard to calculate; Although the pressure acting areas on the compression valve unit in the foot valve assembly are continuous, as shown in Figs. 3b and c, the nonlinear-decreasing-pressure laws on the inner and outer annuli are also difficult to solve. To be practical and cost-effective in engineering problem solving, here employs the following modelling scheme.

(1) Theoretically solve out the shim pack deflection under a uniform pressure; Define an equivalent-pressure correction factor for the same law to estimate the shim pack deflection under non-uniform pressure conditions.

(2) Calculate the shim pack deflections under the above two pressure conditions respectively, by using the FEA approach; Validate the theoretical law of the shim pack deflection under a uniform pressure, then identify the equivalent-pressure correction factor for estimating the shim pack deflection under real pressure conditions.

(3) Model the pressure-flow characteristics of the valve system.

2.2.2 Modelling the shim pack deflection

Figure 4a illustrates the bending model of a single annular disk with a constant thickness h, when clamped at the inner edge r_n and free at the outer edge r_w and under a uniform pressure P. In the polar coordinate system with the pole at the disk centre and polar radius coincides with the disk radius r, a curved surface differential equation depicting the elastic deflection $w(r)$ of the annular disk, can be deduced [15, 16] as

$$K_w\left[\frac{d^2}{dr^2}+\frac{1}{r}\frac{d}{dr}\right]\left[\frac{dw^2}{dr^2}+\frac{1}{r}\frac{dw}{dr}\right]=P \tag{1}$$

Where the bending stiffness K_w of the annular disk is given by

$$K_w=\frac{Eh^3}{12(1-\nu^2)} \tag{2}$$

Eq. (2) indicates that for a given annular disk, the bending stiffness is a constant.

General solution of Eq. (1) is given by

$$w(r)=C_1\ln r+C_2r^2\ln r+C_3r^2+C_4+w^* \tag{3}$$

Where the sum of the first four members is the general solution of the corresponding homogeneous equation of Eq. (1) and w^* is a particular solution of Eq. (1). Because K_w and P are all independent of r, as shown in Eq. (1), if assuming that $w^*=C^5r_4$, then, substituting $w^*=C^5r_4$ into Eq. (1) and solving out to get

$$w^*=\frac{P}{64K_w}r^4=\frac{3(1-\nu^2)}{16E}\frac{P}{h^3}r^4 \tag{4}$$

Thus, the general solution of Eq. (1) can be further described as

$$w(r)=C_1\ln r+C_2r^2\ln r+C_3r^2+C_4+\frac{3(1-\nu^2)}{16E}\frac{P}{h^3}r^4 \tag{5}$$

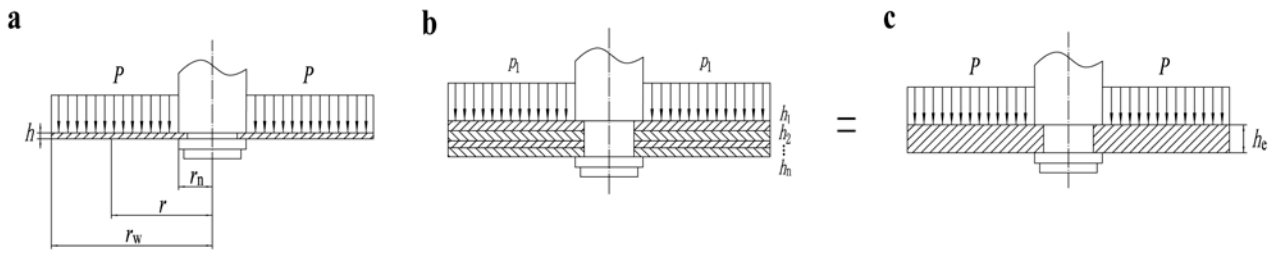

Fig. 4. (a) A single annular disk with constant thickness clamped at the inner edge and free at the outer edge under uniform pressure, (b) A shim pack employing multiple annular disks with the same boundary and uniform pressure conditions but different thicknesses, (c) An single annular disk with an equivalent thickness h_e which is expected to be a substitution of the shim pack.

In order to solve out the constants C_1, C_2, C_3 and C_4 in Eq. (5), here deduces the following equations according to the boundary conditions of the annular disk, which is clamped at the inner edge and free at the outer edge, as shown in Fig. 4a.

(1) Boundary condition of displacement at the inner edge is $w(r)\big|_{r=r_n} = 0$, so substituting r_n into Eq. (5) to get

$$C_1 \ln r_n + C_2 r_n^{\,2} \ln r_n + C_3 r_n^{\,2} + C_4 + \frac{3(1-\nu^2)}{16E}\frac{P}{h^3} r_n^{\,4} = 0 \tag{6}$$

(2) Boundary condition of velocity at the inner edge is $\left.\frac{dw}{dr}\right|_{r=r_n} = 0$, so finding derivative of Eq. (5) at $r=r_n$ will have

$$C_1 \frac{1}{r_n} + C_2 (2r_n \ln r_n + r_n) + 2C_3 r_n + \frac{3(1-\nu^2)}{4E}\frac{P}{h^3} r_n^{\,3} = 0 \tag{7}$$

(3) Boundary condition of bending force at the outer edge is $F_b\big|_{r=r_w} = 0$, so it is able to deduce the following differential equation

$$-K_w \frac{d}{dr}\left[\frac{d^2 w}{dr^2} + \frac{1}{r}\frac{dw}{dr}\right]\Bigg|_{r=r_w} = 0 \tag{8}$$

Thus, substituting Eq. (5) into Eq. (8) to concretely get

$$C_2 \frac{4}{r_w} + \frac{6(1-\nu^2)}{E}\frac{P}{h^3} r_w = 0 \tag{9}$$

(4) Boundary condition of bending torque at the outer edge is $M_b\big|_{r=r_w} = 0$, so it is easy to deduce the following differential equation

$$-K_w \left[\frac{d^2 w}{dr^2} + \nu \frac{1}{r}\frac{dw}{dr}\right]\Bigg|_{r=r_w} = 0 \tag{10}$$

Substituting Eq. (5) into Eq. (10) to get

$$C_1\frac{(\nu-1)}{r_w{}^2}+C_2[2(\nu+1)\ln r_w+(\nu+3)]+2C_3(\nu+1)+\left[\frac{3(1-\nu^2)(3+\nu)}{4E}\right]\frac{P}{h^3}r_w{}^2=0 \tag{11}$$

Combining Eqs. (6), (7), (9) and (11) to solve out the constant coefficients C_1~C_4 of the general solution of the homogeneous equation of Eq. (1), as

$$C_1=-\left[B_2+\frac{r_n{}^2}{B_4}(B_2+B_3)\right]\left(\frac{P}{h^3}\right) \tag{12}$$

$$C_2=B_1\left(\frac{P}{h^3}\right) \tag{13}$$

$$C_3=\left[\frac{(B_2+B_3)}{2B_4}\right]\left(\frac{P}{h^3}\right) \tag{14}$$

and $$C_4=\left[B_5+B_2\ln r_n+\frac{(B_2+B_3)r_n{}^2(2\ln r_n-1)}{2B_4}\right]\left(\frac{P}{h^3}\right) \tag{15}$$

Where the constant coefficients B_1~B_5 are

$$B_1=-\left[\frac{3(1-\nu^2)r_w{}^2}{2E}\right] \tag{16}$$

$$B_2=\left[\frac{3(1-\nu^2)r_n{}^2}{2E}\right]\left[\frac{r_n{}^2}{2}-r_w{}^2(2\ln r_n+1)\right] \tag{17}$$

$$B_3=\left[\frac{3(1-\nu^2)r_w{}^4}{2E(\nu-1)}\right]\left[2(\nu+1)\ln r_w+\frac{(\nu+3)}{2}\right] \tag{18}$$

$$B_4=\left[\frac{(\nu+1)}{(\nu-1)}r_w{}^2-r_n{}^2\right] \tag{19}$$

and $$B_5=\left[\frac{3(1-\nu^2)r_n{}^2(8r_w{}^2\ln r_n-r_n{}^2)}{16E}\right] \tag{20}$$

Therefore, the general solution Eq. (5) can be further described as

$$\begin{aligned}w(r)&=C_1\ln r+C_2r^2\ln r+C_3r^2+C_4+\left[\frac{3(1-\nu^2)}{16E}r^4\right]\frac{P}{h^3}\\&=C_w\frac{P}{h^3}\end{aligned} \tag{21}$$

Where $$\begin{aligned}C_w=&\frac{3(1-\nu^2)}{16E}r^4+\left[B_1\ln r+\frac{(B_2+B_3)}{2B_4}\right]r^2-\left[B_2+\frac{r_n{}^2}{B_4}(B_2+B_3)\right]\ln r\\&+\left[B_5+B_2\ln r_n+\frac{(B_2+B_3)r_n{}^2(2\ln r_n-1)}{2B_4}\right]\end{aligned} \tag{22}$$

Equation (22) indicates that, for a given annular disk, for parameters r_n, r_w, E and ν are all constants, C_w is a function only of the radius r, in other words, C_w is independent of the pressure P and the disk thickness h. Thus, C_w is an intrinsic characteristics of the disk and thus named as the disk deflection coefficient.

Thus, for a shim pack employs multiple annular disks with the same r_n, r_w, E and ν but different thicknesses $h_1, h_2, \ldots h_n$, as shown in Fig. 4b, if assuming that a single annular disk, with the same r_n, r_w, E and ν but an equivalent thickness h_e (Fig. 4c), could be a substitution of the shim pack in Fig. 4b, then it has

$$w(r) = C_w \frac{p_1}{h_1^3} = C_w \frac{p_2}{h_2^3} = \ldots = C_w \frac{p_n}{h_n^3} = C_w \frac{P}{h_e^3} \tag{23}$$

and $$F_b = p_1 A_a + p_2 A_a + \ldots + p_n A_a = P A_a \tag{24}$$

Eq. (23) indicates that in Figs. 4b and c, every disk has the same deflection coefficient C_w and the same disk deflection; Eq. (24), however, indicates that the sum of the bending forces of all the disks (Fig. 4b) equals to the bending force of the equivalent disk (Fig. 4c).

Therefore, combining Eqs. (23) and (24) to solve out the deflection of a shim pack, as

$$w(r) = C_w \frac{P}{h_e^3} \tag{25}$$

Where $$h_e = \sqrt[3]{h_1^3 + h_2^3 + \ldots + h_n^3} \tag{26}$$

By referring to Eq. (26), the equivalent thicknesses of the shim packs of the piston extension valve, the piston compression valve and the compression valve unit in the foot valve assembly, are deduced as

$$h_{e1} = \sqrt[3]{3h_2^3 + 4h_3^3} \tag{27}$$

$$h_{e2} = \sqrt[3]{4(h_1^3 + h_2^3)} \tag{28}$$

and $$h_{e3} = \sqrt[3]{8h_4^3} = 2h_4 \tag{29}$$

Equation (25) is able to perform the deflection calculation of a shim pack under a uniform pressure; however, to perform that of a shim pack under complex pressure conditions demonstrated in Figs. 2 and 3, here uses the following estimation equation

$$w(r) = C_w \frac{P_e}{h_e^3} = C_w \frac{(C_e P)}{h_e^3} = C_e C_w \frac{P}{h_e^3} \tag{30}$$

Eq. (30) assumes that the deflection of a shim pack under non-uniform pressures equals to that of the same shim pack under an equivalent uniform pressure P_e, so if defining $P_e = C_e P$, then C_e is an equivalent-pressure correction factor.

2.2.3 Validation and parameter identification of the shim pack deflection theory using FEA approach

Based on Eq. (25) and the parameters and values list in Table 1, the shim pack deflections under uniform pressures of the three damping valves are calculated and shown in Fig. 5; Fig. 5 demonstrates the nonlinear elastic deflecting behaviour of the shim packs under uniform pressures.

Table 1
Parameters and values used in the shim pack deflection calculation.

Parameter	Value	Parameter	Value
E	2.00×10^{11} Pa	r_{n23}	1.60×10^{-2} m
h_1	3.05×10^{-4} m	r_{n4}	5.00×10^{-3} m
h_2	4.05×10^{-4} m	r_{w12}	2.90×10^{-2} m
h_3	4.10×10^{-4} m	r_{w23}	2.90×10^{-2} m
h_4	3.05×10^{-4} m	r_{w4}	1.10×10^{-2} m
r_{n12}	1.60×10^{-2} m	v	3.00×10^{-1}

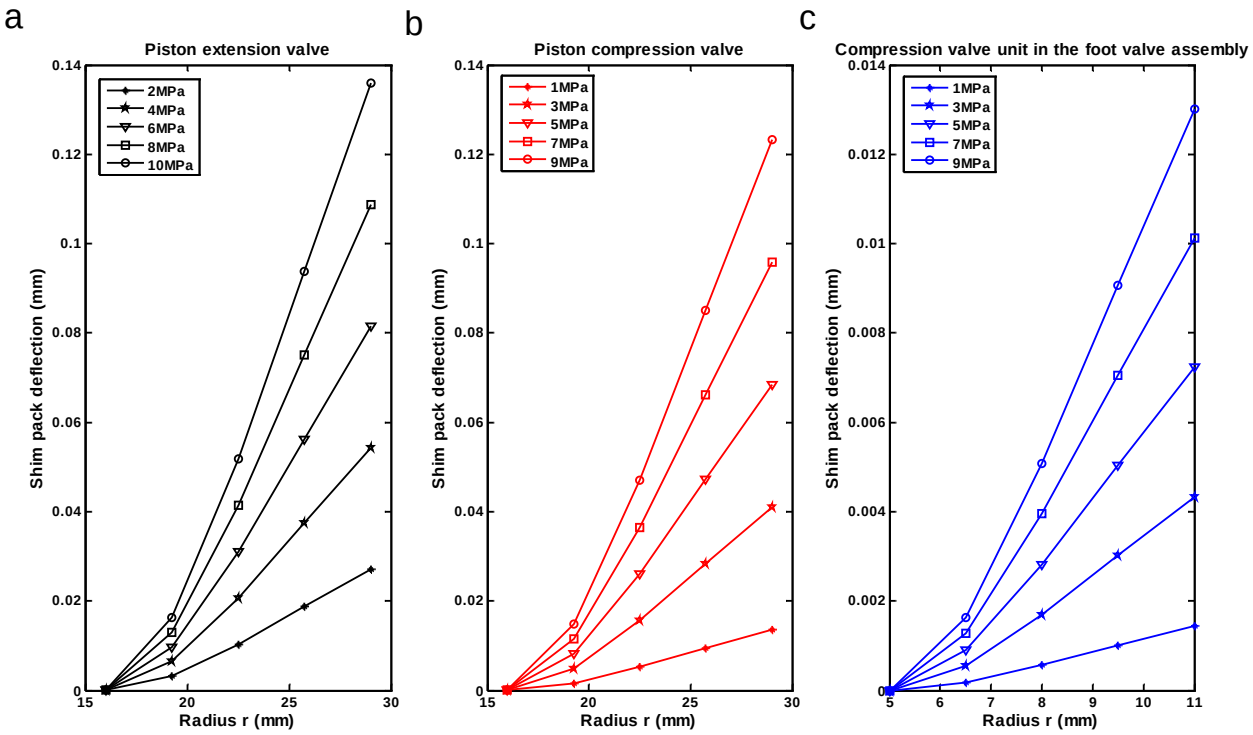

Fig. 5. Theoretical calculation results of the shim pack deflection under uniform pressure of the piston extension valve (a), the piston compression valve (b) and the compression valve unit in the foot valve assembly (c).

To validate the deflection theory and calculation results of the shim packs under uniform pressures introduced above, here employs the ANSYS software to perform corresponding finite element analyses. As an example, Fig. 6 demonstrates FEA of the shim pack deflection of the piston extension valve under a uniform pressure of P=6 MPa.

Tables 2-4 compare the theoretical calculation results with the FEA results of the maximum deflections of the three damping valve shim packs under uniform pressures, and show that the two kinds of results agree with each other with very small relative errors. Thus, the deflection theory of a shim pack under uniform pressure, which is basically described by Eq. (25), is validated.

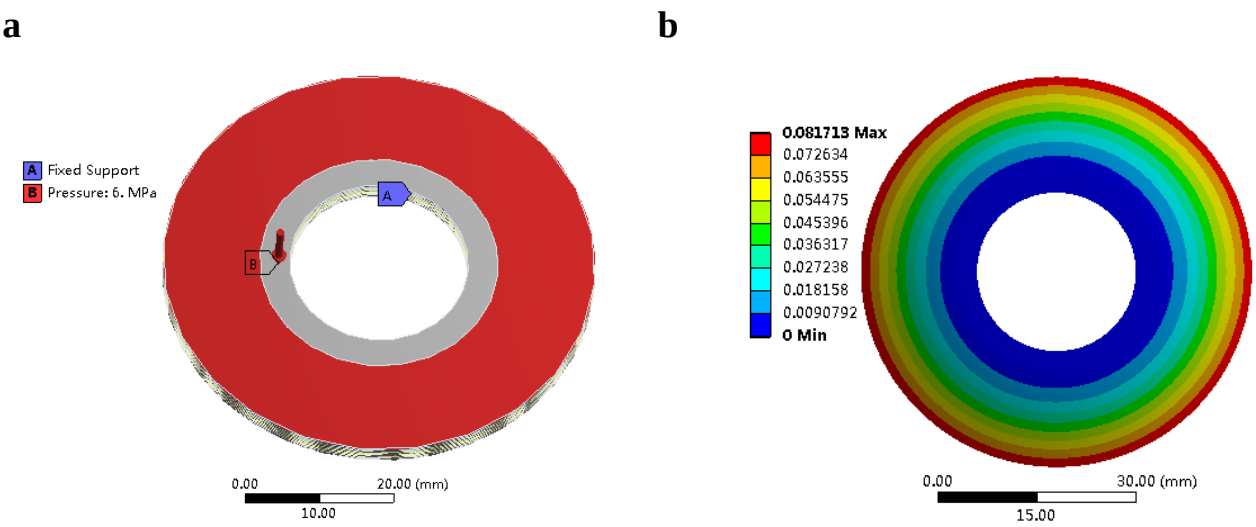

Fig. 6. FEA of the shim pack deflection of the piston extension valve: (a) loading plot of the shim pack under a uniform pressure of P=6 MPa, (b) the obtained contour plot of the shim pack deflection.

Table 2
The maximum shim pack deflection and equivalent-pressure correction factor of the piston extension valve.

	2 MPa	**4 MPa**	**6 MPa**	**8 MPa**	**10 MPa**
Theoretical result under uniform pressure (mm)	0.027200	0.054400	0.081600	0.108800	0.136000
FEA result under uniform pressure (mm)	0.027238	0.054475	0.081713	0.108950	0.136190
*FEA result under real pressure conditions (mm)	0.005899	0.011798	0.017697	0.023596	0.029495
Equivalent-pressure correction factor C_{e1}	0.2169	0.2169	0.2169	0.2169	0.2169

* In each discrete pressure acting area, only the central circle undergoes uniform pressure.

Table 3
The maximum shim pack deflection and equivalent-pressure correction factor of the piston compression valve.

	1 MPa	**3 MPa**	**5 MPa**	**7 MPa**	**9 MPa**
Theoretical result under uniform pressure (mm)	0.013700	0.041100	0.068500	0.095900	0.123300
FEA result under uniform pressure (mm)	0.013727	0.041182	0.068636	0.096091	0.123550
*FEA result under real pressure conditions (mm)	0.002741	0.008223	0.013704	0.019186	0.024668
Equivalent-pressure correction factor C_{e2}	0.2	0.2	0.2	0.2	0.2

* In each discrete pressure acting area, only the central circle undergoes uniform pressure.

Table 4
The maximum shim pack deflection and equivalent-pressure correction factor of the compression valve in the foot valve assembly.

	1 MPa	**3 MPa**	**5 MPa**	**7 MPa**	**9 MPa**
Theoretical result under uniform pressure (mm)	0.001450	0.004340	0.007230	0.010120	0.013020
FEA result under uniform pressure (mm)	0.0014503	0.004351	0.007251	0.010152	0.013053
*FEA result under real pressure conditions (mm)	0.001195	0.003586	0.005977	0.008368	0.010758
Equivalent-pressure correction factor C_{e3}	0.8263	0.8265	0.8265	0.8266	0.8265

* Only the middle big annulus undergoes uniform pressure.

To identify the equivalent-pressure correction factor C_e defined in Eq. (30), here continues to perform FEA of the deflections of the three valve shim packs under real pressure conditions as that illustrated in Figs. 2 and 3.

As examples, Fig. 7 demonstrates the loading plots and the obtained deflection contour plots of the shim packs of the piston extension valve and the compression valve unit in the foot valve assembly.

Fig. 7a shows that the piston extension valve shim pack is subjected to six identical discrete pressure loadings. In each pressure acting area, the central circle undergoes a uniform pressure of P=2 MPa, and the outer rectangle undergoes an assumed quadratic nonlinear-decreasing pressure from P=2 MPa to zero. Fig. 7a is actually an approximate loading model of the piston extension valve shim pack, however, for the area outside the central circle is small, Fig. 7a might not lose accuracy in engineering calculation.

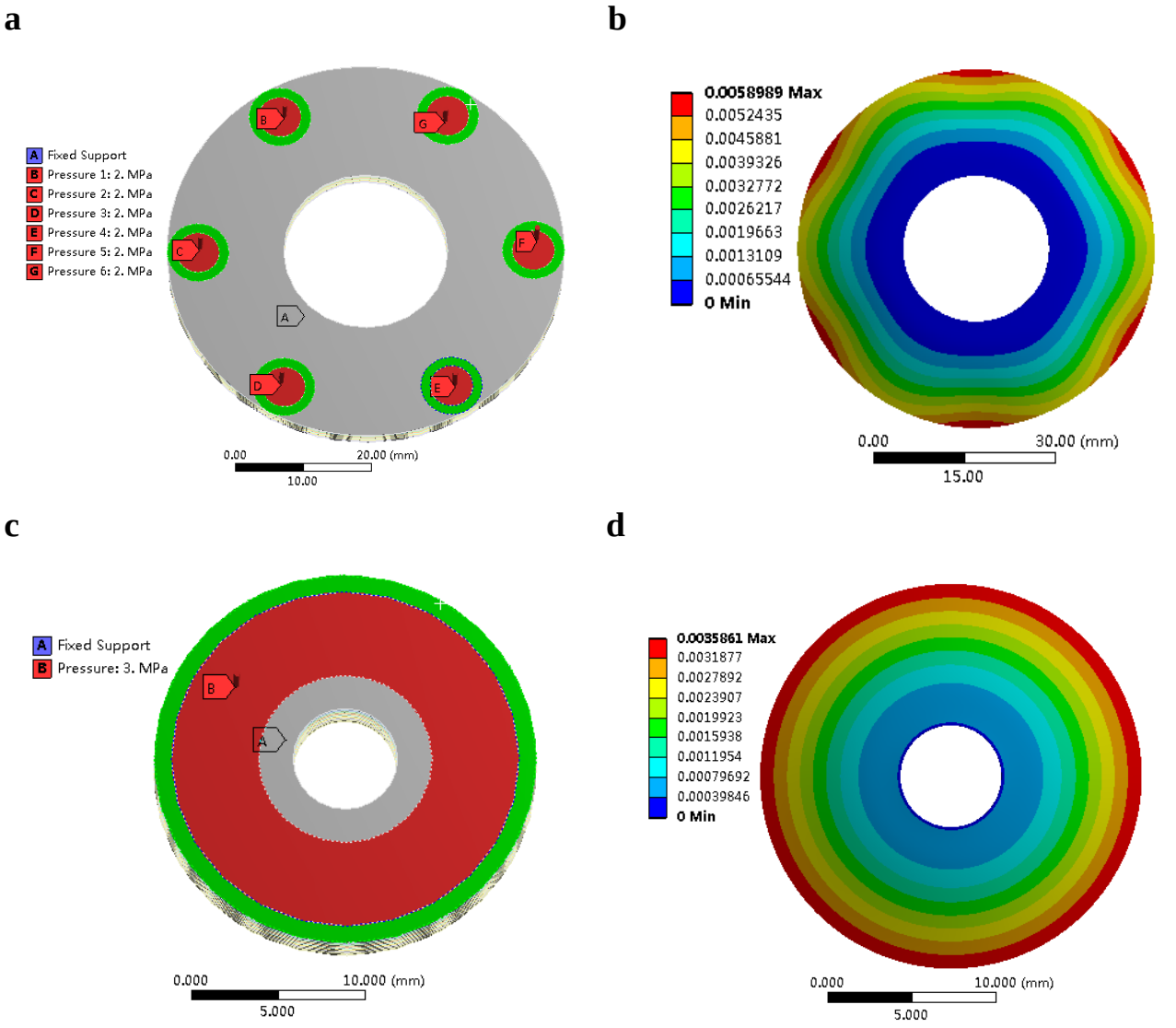

Fig. 7. FEA of shim pack deflection under non-uniform pressure conditions: the loading plot (a) and the obtained deflection contour plot (b) of the piston extension valve shim pack; the loading plot (c) and the obtained deflection contour plot (d) of the shim pack of the compression valve unit in the foot valve assembly.

Similarly, Fig. 7c, shows the approximate loading conditions of the shim pack of the compression valve unit in the foot valve assembly. The middle big annulus is subjected to a uniform pressure of P=3 MPa, and the small outer annulus is subjected to an assumed quadratic nonlinear-decreasing pressure from P=3 MPa to zero, for the inner annulus is pressed against the rigid backing plate, it is fixed in the analysis.

Tables 2-4 also list the concrete FEA results of the maximum deflections of the three damping valve shim packs under approximate real pressure conditions. Thus, by using Eq. (30) and the datum in Tables 2-4, it is easy to identify the equivalent-pressure correction factors for the three damping valves, if using the mean value, then it has C_{e1}=0.2169, C_{e2}=0.2 and C_{e3}=0.8265.

2.2.4 Pressure-flow characteristics of the valve system

With the validated and parameter identified shim pack deflection theory, and by referring to Figs. 1-3, it is easy to write the dynamic pressure-flow characteristics of the damping valve system, as

$$Q_{\text{valve}}=\begin{cases} C_{\text{d1}}\left(\frac{\pi}{4}d_{\text{c}}\right)^2\left(\frac{2}{\rho}P\right)^{1/2}+C_{\text{d2}}\left(2\pi r_{\text{w23}}C_{\text{e1}}C_{\text{w}}\Big|_{r=r_{\text{w23}}}\frac{P}{h_{\text{e1}}{}^3}\right)\left(\frac{2}{\rho}P\right)^{1/2}, \text{ if } \dot{x}_{\text{r}}(t)\geq 0, \\ C_{\text{d1}}\left(\frac{\pi}{4}d_{\text{c}}\right)^2\left(\frac{2}{\rho}P\right)^{1/2}+C_{\text{d2}}\left(2\pi r_{\text{w12}}C_{\text{e2}}C_{\text{w}}\Big|_{r=r_{\text{w12}}}\frac{P}{h_{\text{e2}}{}^3}\right)\left(\frac{2}{\rho}P\right)^{1/2} \\ \qquad\qquad +C_{\text{d2}}\left(2\pi r_{\text{w4}}C_{\text{e3}}C_{\text{w}}\Big|_{r=r_{\text{w4}}}\frac{P}{h_{\text{e3}}{}^3}\right)\left(\frac{2}{\rho}(P-P_{\text{b}})\right)^{1/2}, \text{ if } \dot{x}_{\text{r}}(t)<0. \end{cases} \tag{31}$$

Where the back pressure in the reservoir P_{b} was given in [13].

2.3. Experimental validation

Damping characteristics of the hydraulic damper was simulated by using the established nonlinear physical in-service model, the simulated key results are shown in Figs. 8, 9 and Table 5. In the simulation, the discharge coefficient of the constant orifice C_{d1} was specified to be 0.72 because the length to diameter ratio [17, 18] of the orifice is between 0.5 and 4, the discharge coefficient of the shim packs C_{d2} was specified to be 0.61 because the deflected shim packs are actually sharp-edged hydraulic valve ports [17, 18]; The diameters of the rod, the piston and the constant orifice are 28 mm, 69.8 mm and 2 mm, respectively; Additionally, values of some key parameters are set to be that in normal conditions, such as the hydraulic oil temperature T=45℃, the entrained air ratio [13] of oil at atmospheric pressure ε_0=0.05%, the accumulated clearance at damper ends $2a$=0 mm, and the rubber attachment stiffness of damper $K_{\text{rubber}}=6\times10^6$ N/m.

For comparison, the bench test results of a sample secondary suspension vertical hydraulic damper are also shown in Figs. 8, 9 and Table 5. The sampled hydraulic damper has just been repaired after a 2×10^5 kM service journey.

Figure 8 demonstrates the nominal-speed characteristics of the hydraulic damper and verifies that the simulation result agrees tolerably well with the test result. Because the sampled hydraulic damper has just been

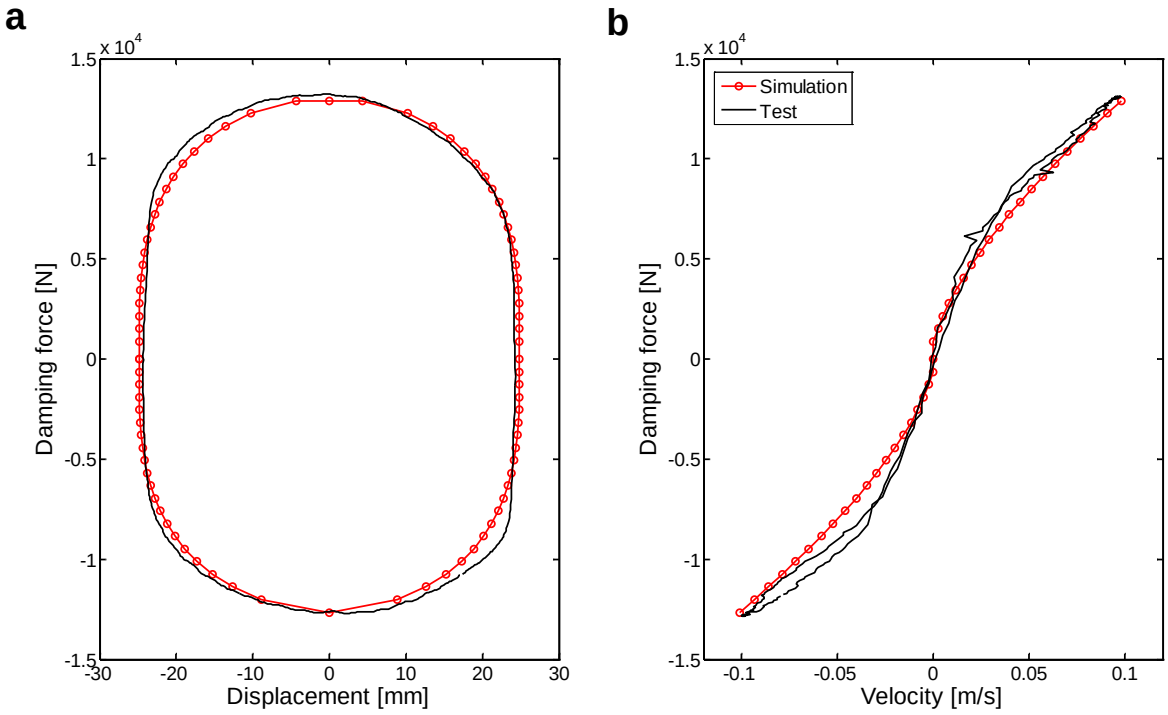

Fig. 8. Nominal-speed force vs. displacement (***F*-*s***) characteristics (a) and force vs. velocity (***F*-*v***) characteristics (b) of the secondary suspension vertical hydraulic damper, with a harmonic excitation of displacement amplitude ± 24.875 mm, frequency 0.64 Hz and velocity amplitude ± 0.1 m/s (other conditions: T=45℃, ε_0=0.05%, 2a=0 mm, K_{rubber}=6×10^6 N/m).

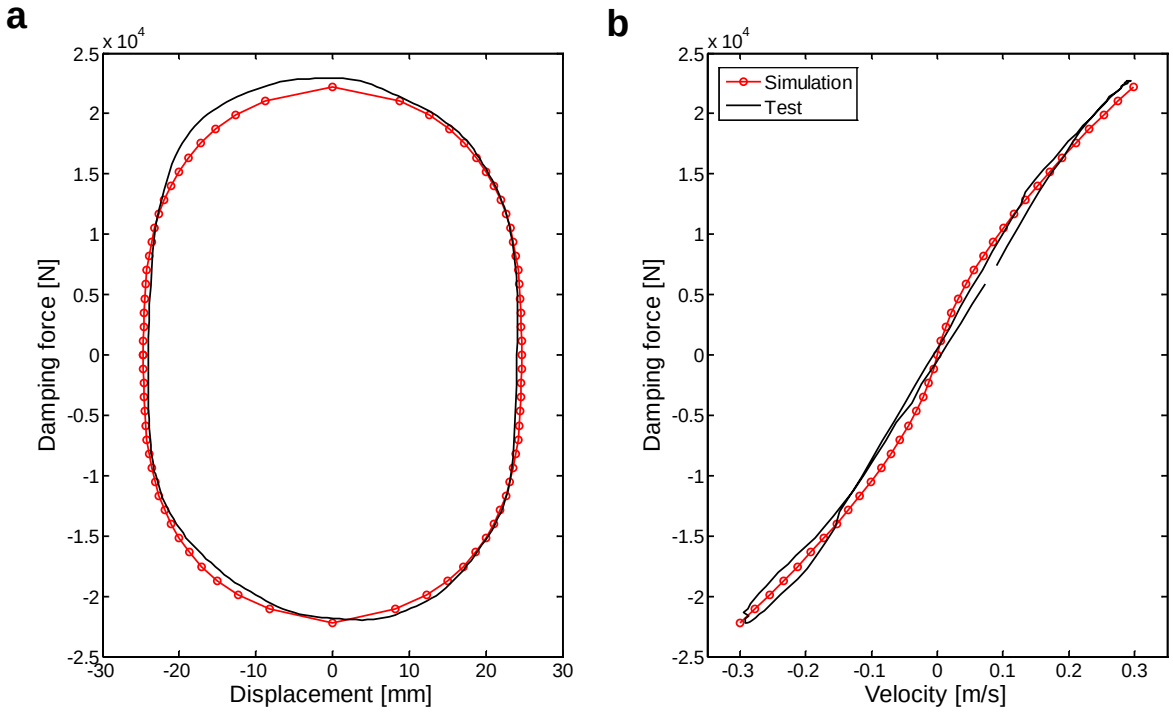

Fig. 9. Maximum-speed ***F*-*s*** characteristics (a) and ***F*-*v*** characteristics (b) of the secondary suspension vertical hydraulic damper, with a harmonic excitation of displacement amplitude ± 24.665 mm, frequency 1.90 Hz and velocity amplitude ± 0.3 m/s (other conditions: T=45℃, ε_0=0.05%, 2a=0 mm, K_{rubber}=6×10^6 N/m).

Table 5
A comparison of the simulation result with the test result in terms of the nominal damping characteristics.

Nominal damping characteristic index	Simulation	Test	Relative error
Damping coefficient (kNs/m)	127.96	131.10	2.39%
Maximum extension damping force (N)	12892	13109	1.66%
Maximum compression damping force (N)	12649	12849	1.56%
Asymmetry rate of the damping force (%)	0.95	1.00	5.00%
Energy absorption in one excitation cycle (Nm)	1022.87	1043.65	1.99%

repaired after a 2×10^5 kM service, when the damper is accelerated, the test damping forces near the maximum extension or compression speeds are prone to be larger than that in normal cases and also seem to be unstable, this phenomenon might be induced by the shim pack fatigue and reassembling issues during the repair process. However, it is reasonable in engineering, and the disagreement is small and tolerable. Additionally, Table 5 also verifies that the nominal damping characteristic indices of simulation and test coincide well with each other, with a maximum relative error of only 5%.

Figure 9 demonstrates the maximum-speed characteristics of the hydraulic damper. In practice, the aim of testing the maximum-speed characteristics of a hydraulic damper is to evaluate the damper quality over its full speed range, such as the linearity of damping coefficient and the stability of the damping forces over that range. In normal cases, the secondary suspension vertical hydraulic damper cannot reach a vibration speed amplitude of v=0.3 m/s at all, however, Fig. 9 shows the maximum-speed damping characteristics of simulation and test also coincide well with each other, and it seems that the biases are reduced due to high-speed effects.

Therefore, it was concluded that the established nonlinear physical in-service damper model captured the damping characteristics of the secondary suspension vertical hydraulic damper over its full speed range, it also validated that the proposed shim pack deflection theory with an equivalent-pressure correction factor and the FEA-based parameter identification approach are effective in engineering.

3. Vehicle system dynamic response

To study rail vehicle dynamic response to the validated nonlinear physical in-service model of its secondary suspension dampers, here upgrades and refines the detailed MBS model of the Chinese electric locomotive SS_9, which was introduced in a previous paper (see Wang et al. [3]), using the current new version of SIMPACK software. The new MBS model, as shown in Fig. 10, has a more detailed configuration and more accurate parameters; In the secondary suspension of SS_9, four vertical and two lateral hydraulic dampers are installed between each bogie frame and the carbody.

Here also uses the parameter estimation and response calculation approach introduced in the previous paper (see Wang et al. [3]). It includes estimating key parameters, such as the in-service effective stiffness K_e, the in-service small mounting clearance $2a$, the saturation velocity V_r or the saturation force F_r, defining a user's damper model in MBS model and calculating the dynamic response using the MBS model.

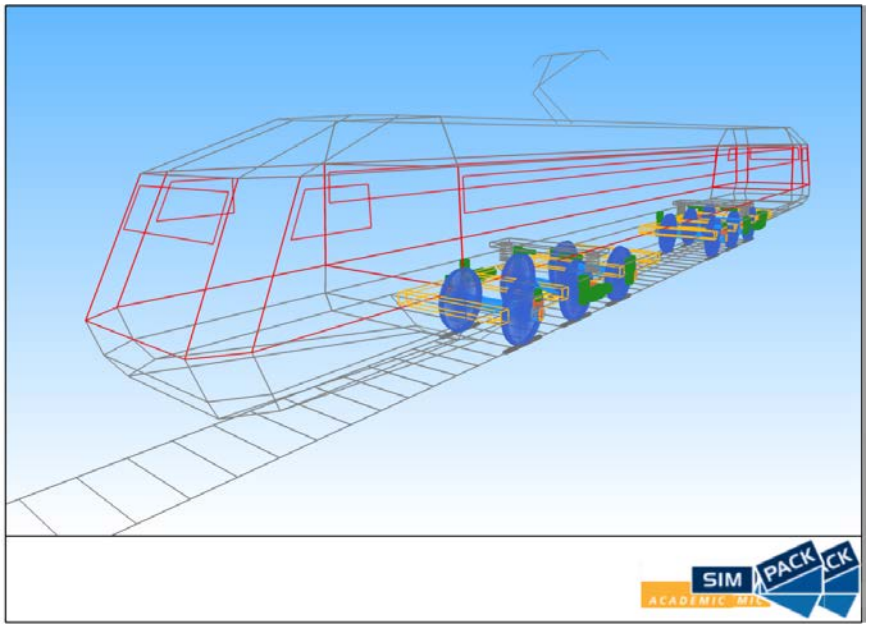

Fig. 10. MBS model for simulating the Chinese electric locomotive SS_9 dynamics.

3.1. Dynamic response on tangent track

3.1.1 Dynamic response to vertical damper parameter variations

Figure 11 shows the stochastic damping characteristics of a secondary suspension vertical hydraulic damper when simulating the vehicle dynamics on tangent track. The small clearance 2*a* between the damper and its two fixing seats is assumed to be 1 mm, which is common in engineering due to structural clearance and lack of maintenance, so the stochastic *F*-*s* performance demonstrates 1 mm dead zone.

Figure 12 gives the results of vehicle ride comfort indices on tangent track versus key parameter variations of its secondary suspension vertical hydraulic dampers. Figs. 12a and b show that vertical ride index W_{zz} increases (it means the vertical ride comfort is getting worse) with the increase of damping coefficient C and saturation velocity V_r of the vertical dampers, so both C and V_r should be appropriately specified, their values should be neither too low which mean being insufficient for vibration reduction, nor too high which are prone to transfer high frequency vibrations; In Fig. 12b, when V_r exceeds 0.05 m/s, which cannot be reached by the maximum vertical vibration speed of the carbody, W_{zz} does not change any more, in other words, if V_r was specified too high, saturation capability of the damper would not function well, and excessive damping forces would not be relieved; Figs. 12a and b also show that both C and V_r of the vertical dampers have hardly any influences on lateral ride comfort index W_{zy} of the vehicle.

Figure 12c demonstrates that W_{zz} decreases (it means the vertical ride comfort is getting better) with the increase of in-service effective stiffness K_e of the vertical dampers, and this effect can be easily interpreted by Fig. 13. Fig. 13a shows that vertical vibration of the carbody is apparently reduced with the increase of K_e, thus, vertical ride comfort of the vehicle is improved; Bode Diagram amplitude-frequency characteristics of the vertical dampers, as shown in Fig. 13b, also illustrate that with the increase of K_e, vibration transfer

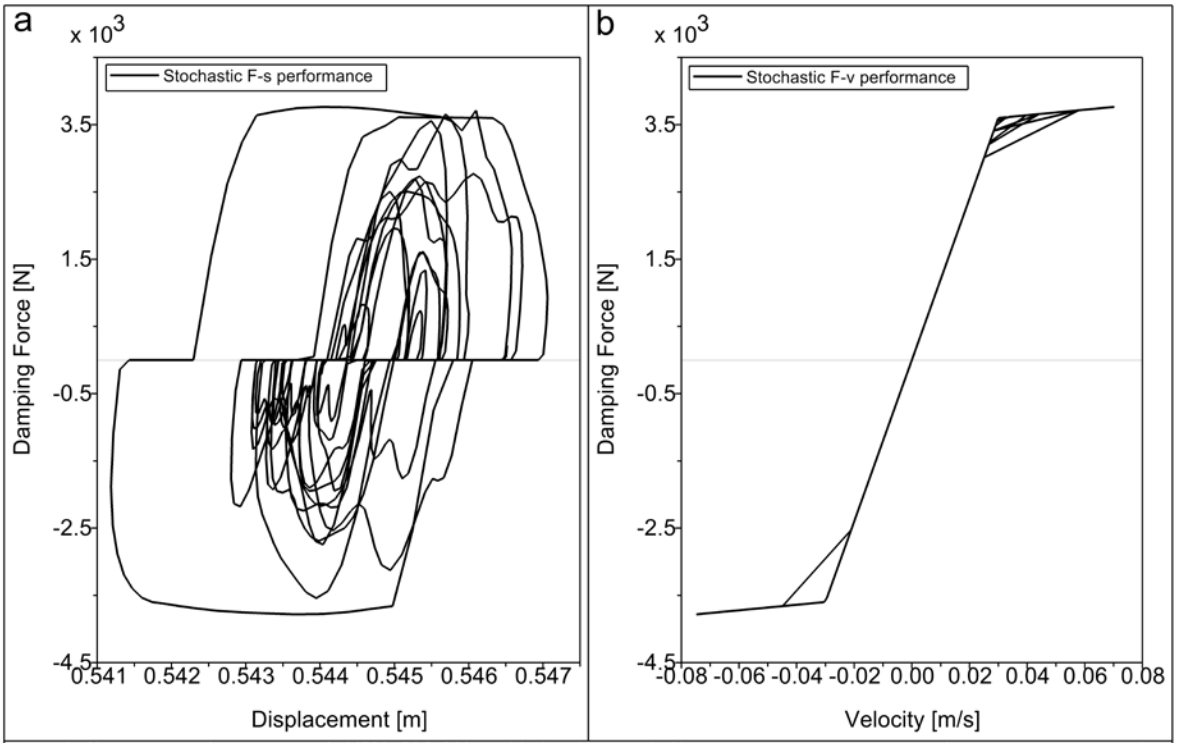

Fig. 11. Stochastic ***F-s*** performance (a) and ***F-v*** performance (b) of a secondary suspension vertical hydraulic damper (Simulation conditions: vehicle speed V=180 km/h, on tangent track with the sixth grade American track irregularities (Am6) excitations (see Wang et al. [3]), simulation time t=5 s; damping coefficient C=120 kNs/m, saturation velocity V_r=0.03 m/s, effective stiffness K_e=8 MN/m, small clearance 2a=1 mm).

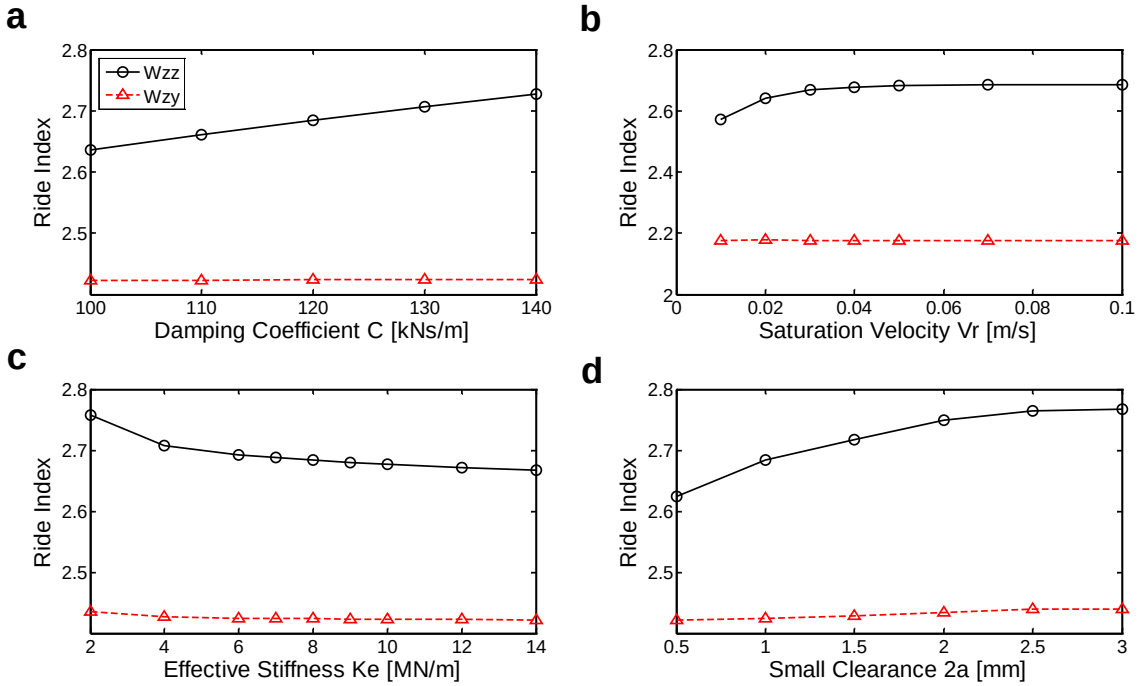

Fig. 12. Vehicle ride comfort indices on tangent track versus key parameter variations of its secondary suspension vertical hydraulic dampers (Simulation conditions: V=180 km/h, on tangent track with Am6 excitations).

characteristics of the vertical dampers are significantly decreased over the main frequency range 0.8-3.4 Hz of the carbody vertical vibrations, vertical ride comfort of the vehicle is therefore improved. However, Fig. 13b also indicates that with the increase of K_e, the vertical dampers are more easily to transfer vibrations over the high frequency range (up to 7 Hz), thus, K_e should not be too high.

In Fig. 12c, vertical ride comfort of the vehicle can be improved by 2.94% when K_e is increased from 2 MN/m to 10 MN/m; Fig. 12c also shows that K_e of the vertical dampers have hardly any influence on lateral ride comfort index W_{zy} of the vehicle.

Figure 12d shows that the small clearance 2*a* between the vertical dampers and their fixing seats has a significant impact on vertical ride comfort of the vehicle. When 2*a* increases from 0.5 mm to 2.5 mm, the vertical ride comfort would deteriorate by 5.29%; when 2*a* exceeds 2.5 mm, the vertical ride index hardly changes because 2*a* reaches the level of carbody vertical vibration amplitudes, in other words, the vertical dampers would not function well when 2*a* exceeds 2.5 mm. Fig. 14 also illustrates that with the increase of 2*a*, carbody vertical vibration acceleration and PSD over the main frequency range 0.8-3.4 Hz would increase significantly, thus, vertical ride comfort of the vehicle would deteriorate remarkably.

Additionally, Fig. 12d shows that with the increase of 2*a*, lateral ride comfort of the vehicle also deteriorate slightly, so this phenomenon indicates that increase of 2*a* has a slight effect on the coupling of carbody vertical and lateral vibrations.

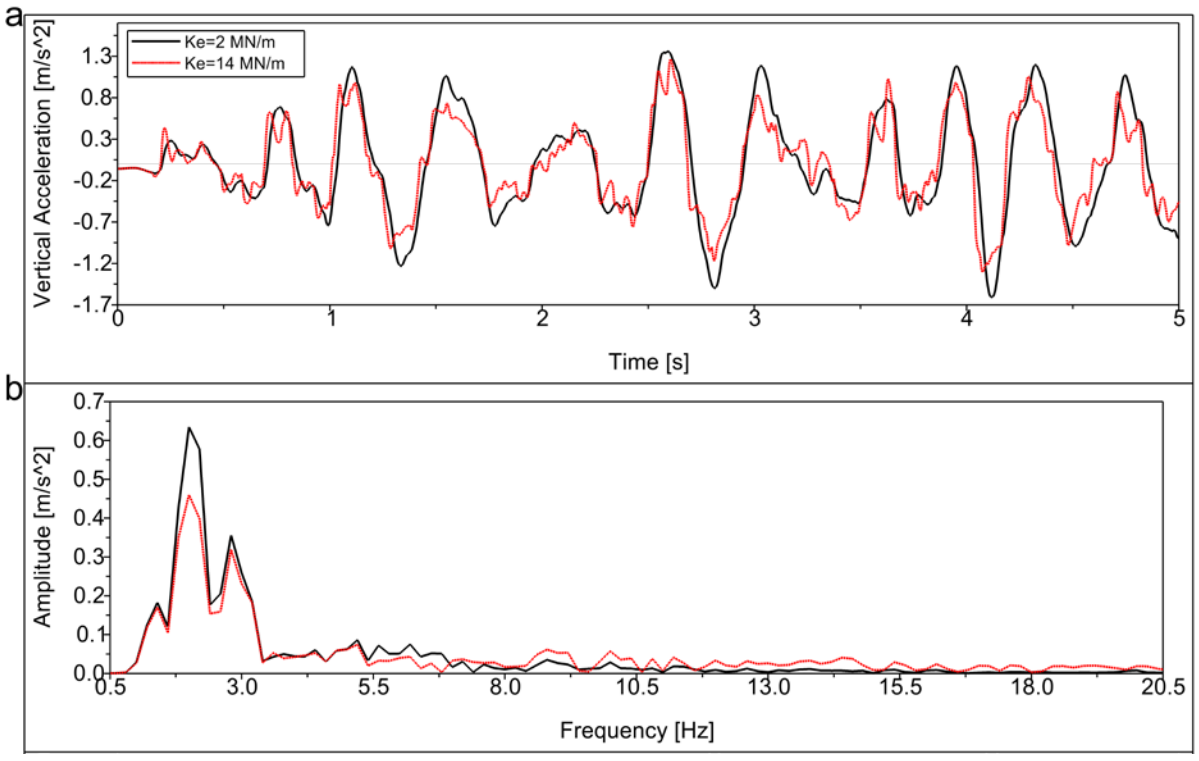

Fig. 13. The influence of in-service effective stiffness K_e of secondary suspension vertical hydraulic dampers on carbody vertical vibration acceleration (a) and pertinent Bode Diagram amplitude-frequency characteristics of the dampers (b) (Simulation conditions: V=180 km/h, on tangent track with Am6 excitations, t=5 s).

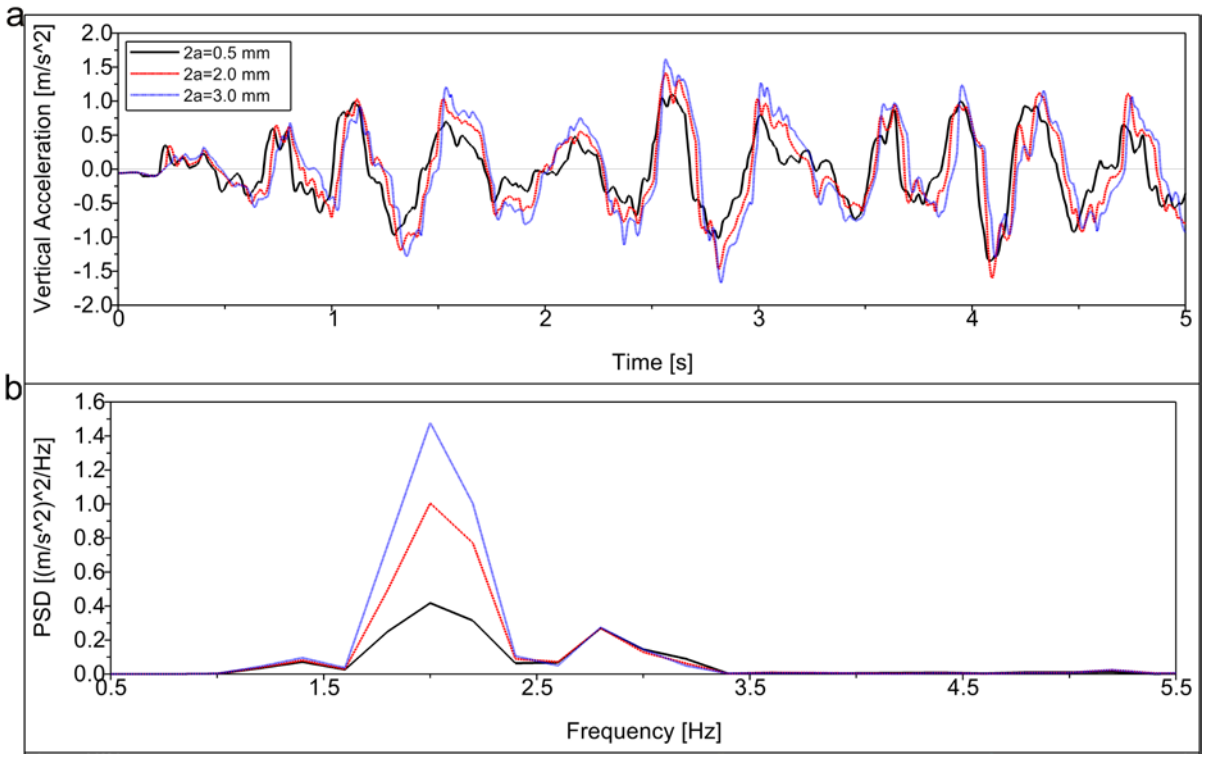

Fig. 14. The influence of in-service small clearance 2*a* between secondary suspension vertical hydraulic dampers and their fixing seats on carbody vertical vibration acceleration (a) and Power Spectrum Density (PSD) (b) (Simulation conditions: *V*=180 km/h, on tangent track with Am6 excitations, *t*=5 s).

3.1.2 Dynamic response to lateral damper parameter variations

Figure 15 gives the results of vehicle ride comfort indices on tangent track versus key parameter variations of its secondary suspension lateral hydraulic dampers. Figs. 15a and b show that C and V_r of the lateral dampers have the similar effects and trends on lateral ride index W_{zy} of the vehicle, as that on vertical ride index W_{zz} by C and V_r variations of the vertical dampers, however, Figs. 15a and b also show that with the increases of C and V_r, vertical ride comfort W_{zz} of the vehicle also deteriorate remarkably, this means that parameter variations of the lateral dampers can contribute a lot to the coupling of carbody lateral and vertical vibrations.

In Fig. 15c, the effect and mechanism of in-service effective stiffness K_e variations of the lateral dampers on lateral ride comfort of the vehicle are similar to that illustrated in Figs. 12c and 13, and lateral ride comfort of the vehicle can be improved by 2.65% when K_e is increased from 2 MN/m to 8 MN/m; K_e variations of the lateral dampers have no obvious influence on vertical ride index of the vehicle.

Figure 15d shows that with the increase of small clearance 2*a* between the lateral dampers and their fixing seats, it seems that the lateral ride comfort has a slight trend of improvement because of less constraints of the lateral dampers to the carbody lateral vibrations, however, this does not mean the small clearance 2*a* is encouraged, 2*a* has negative influences on other dynamic performance of the vehicle, such as on the vehicle stability during curve negotiation. Fig. 15d shows that 2*a* variations of the lateral dampers also have influence on

vertical ride index of the vehicle system.

In general, for the secondary suspension lateral dampers, appropriate C and V_r should be specified during the vehicle design stage, a high value of in-service K_e should be guaranteed for vibration reduction and 2a should be avoided. Thus, regular maintenance works are essential to avoid air entrainment in the working fluid and looseness of the damper fixings.

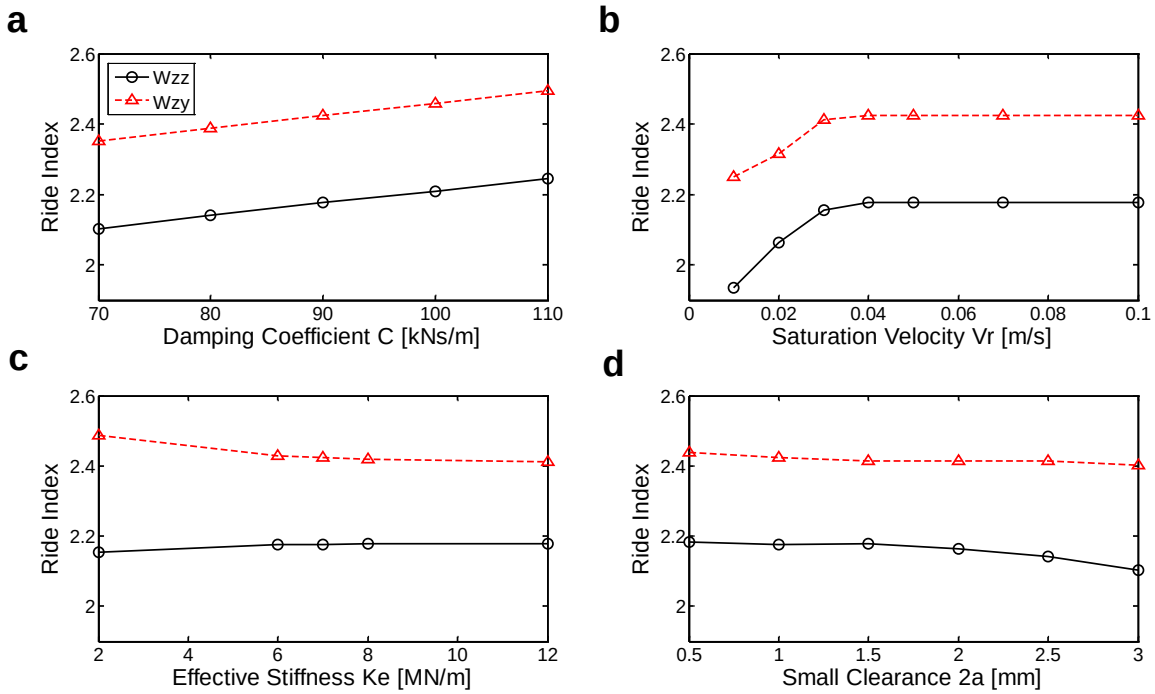

Fig. 15. Vehicle ride comfort indices on tangent track versus key parameter variations of its secondary suspension lateral hydraulic dampers (Simulation conditions: V=180 km/h, on tangent track with Am6 excitations).

3.2. Dynamic response during curve negotiation

Figure 16 shows the stochastic damping characteristics of the secondary suspension lateral hydraulic dampers when simulating the vehicle dynamics during curve negotiation; Fig. 17 gives the vehicle dynamic indices during curve negotiation versus key parameter variations of its secondary suspension lateral hydraulic dampers.

Rail vehicle ride comfort during curve negotiation is usually assessed by centrifugal acceleration of the carbody [19, 20], and Fig. 17 shows that key parameter variations of the lateral dampers have almost no influences on root mean square centrifugal acceleration RMS_A_y of the carbody.

Figures 17a, b and c show that parameter variations of C, V_r and K_e of the lateral dampers all lead to limited fluctuations of the vehicle dynamic indices during curve negotiation, including the root mean square derailment coefficient RMS_D_c of the leading wheel-rail pair, the root mean square total wear number RMS_W_n and the root mean square wheelset-rail lateral shift force RMS_F_y of the leading wheelset.

Figure 17d shows that increasing 2a within usual range in practice would lead to considerable increase of the root mean square derailment coefficient RMS_D_c of the leading wheelset. For example, when 2a increases from

0.5 mm to 2 mm, RMS_D_c would increase by 9.28%, in other words, the increase of small clearance 2*a* between the lateral dampers and their fixing seats would significantly increase the derailment risk of the rail vehicle during curve negotiation. This effect can also be observed and interpreted by Fig. 18.

Figure 18a demonstrates that larger derailment coefficient occurs more frequently when 2*a* becomes larger, and Fig. 18b also indicates that over the main frequency range below 1 Hz of derailment, transfer characteristics of the lateral dampers with larger value of 2*a* increase obviously.

Generally speaking, key parameter variations of the secondary suspension lateral hydraulic dampers mainly influence ride comfort of the rail vehicle, but also have some impacts on the vehicle curve negotiation stability. Although most of the parameter variations of the lateral dampers lead to limited fluctuations of the vehicle dynamic indices during curve negotiation, as shown in Fig. 17, the results are valuable and instructive in parameter optimal specification of the hydraulic dampers.

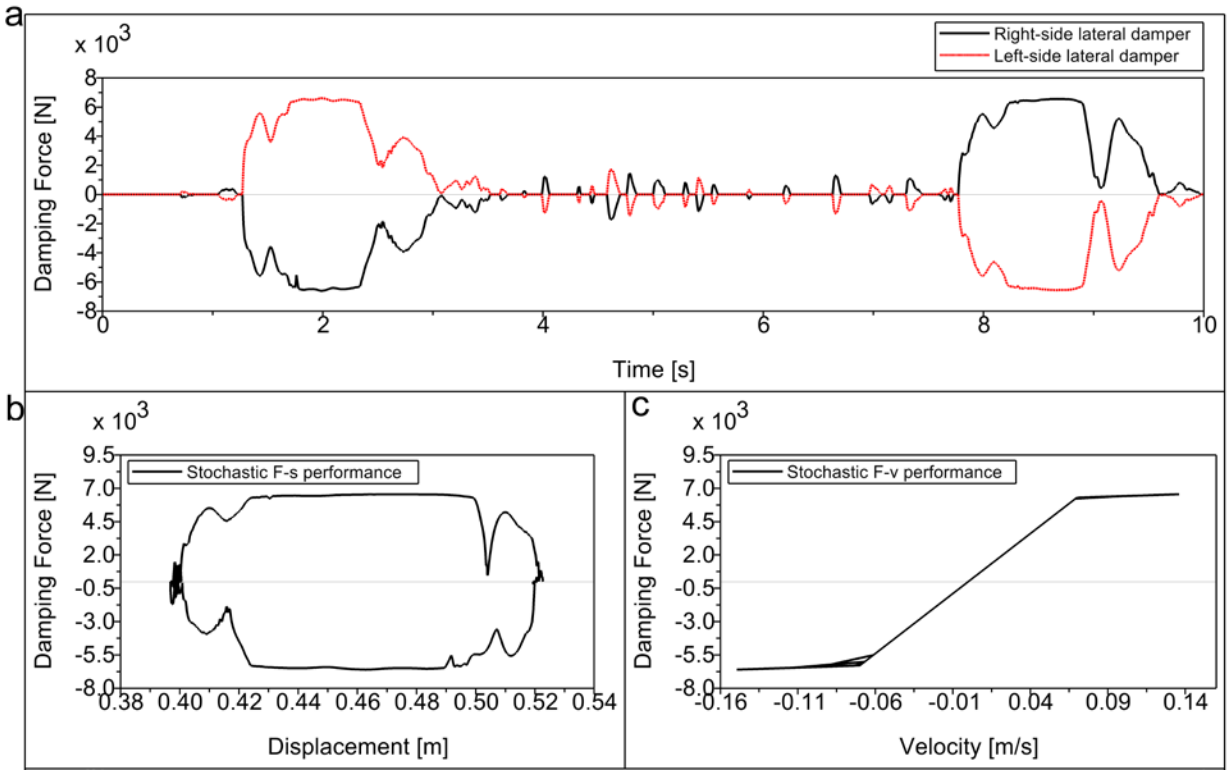

Fig. 16. During curve negotiation, damping force profiles (***F-t***) of the two secondary suspension lateral hydraulic dampers of the front bogie (a), Stochastic ***F-s*** performance (b) and ***F-v*** performance (c) of the right-side lateral damper (Simulation conditions: *V*=100 km/h, curve negotiation with Am6 excitations, curve radius *R*=200 m, outer rail super-elevation 0.12 m, *t*=10 s; *C*=90 kNs/m, V_r=0.07 m/s, K_e=7 MN/m, 2*a*=1 mm).

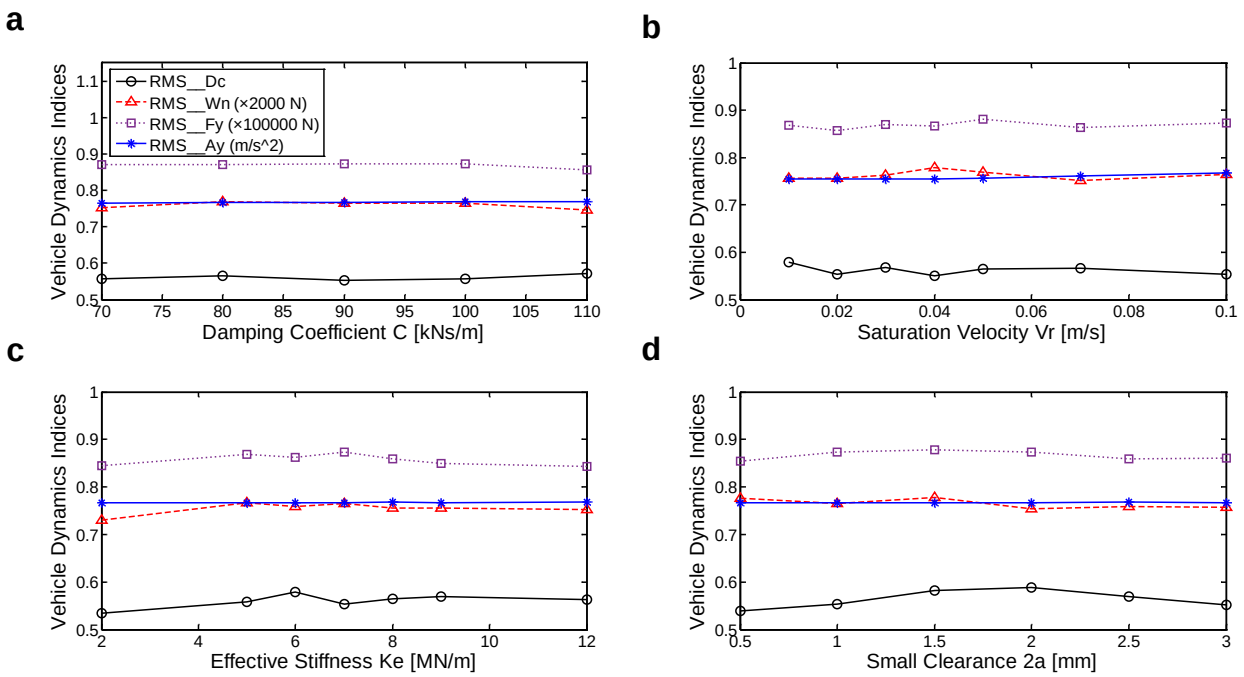

Fig. 17. Vehicle dynamic indices during curve negotiation versus key parameter variations of its secondary suspension lateral hydraulic dampers (Simulation conditions: *V*=100 km/h, curve negotiation with Am6 excitations, curve radius *R*=200 m, outer rail super-elevation 0.12 m, *t*=10 s).

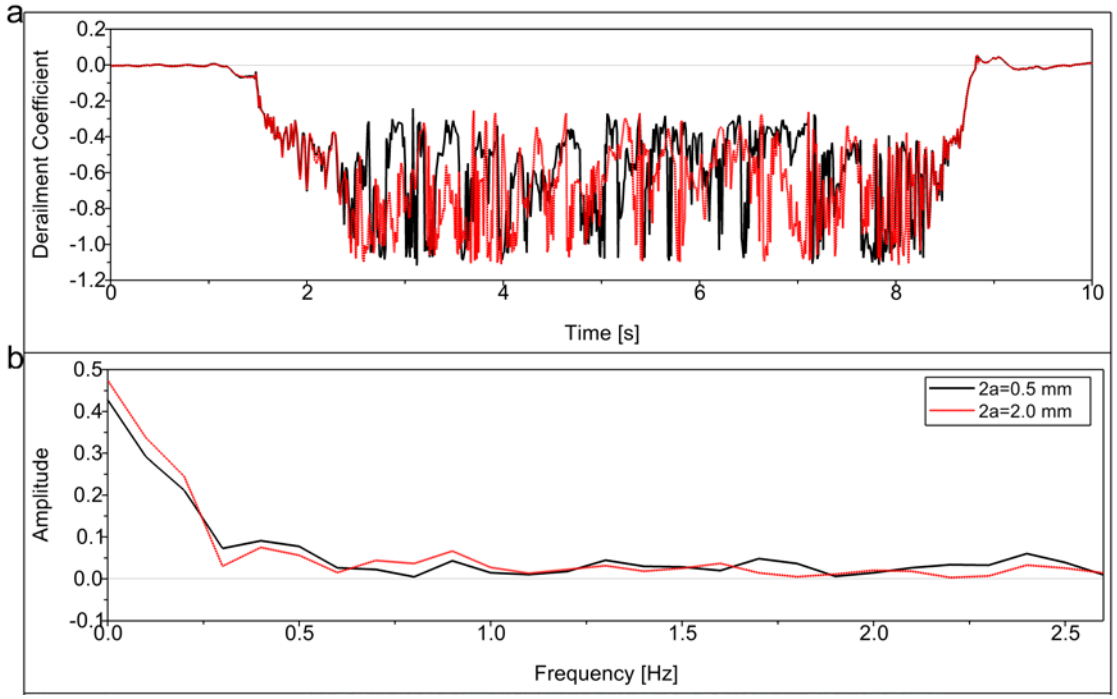

Fig. 18. The influence of in-service small clearance 2*a* between secondary suspension lateral hydraulic dampers and their fixing seats on derailment coefficient of the leading wheel-rail pair during curve negotiation (a) and pertinent Bode Diagram amplitude-frequency characteristics of the dampers (b) (Simulation conditions: *V*=100 km/h, curve negotiation with Am6 excitations, curve radius *R*=200 m, outer rail super-elevation 0.12 m, *t*=10 s).

4. Conclusions

(1) A detailed nonlinear physical in-service model was built assisted by FEA approach for the secondary suspension vertical hydraulic damper with shim-pack-type valves, followed comparison of simulation and test results proves the established damper model captured the nonlinear damping characteristics over a full velocity range, and thus also proves that the proposed shim pack deflection theory with an equivalent-pressure correction factor and the FEA-based parameter identification approach are effective.

(2) Key in-service parameter variations of the vertical damper mainly influence the vertical ride comfort, and that of the lateral damper mainly influence the lateral ride comfort. However, most of the parameter variations of the lateral damper contribute a lot to the coupling of carbody lateral and vertical vibrations, and therefore have also significant influences on the vertical ride comfort. Additionally, key in-service parameter variations of the lateral damper also have some impacts on the vehicle curve negotiation stability.

(3) Both C and V_r of the secondary suspension hydraulic dampers should be optimally specified, their values should be neither too low nor too high; a high value of in-service K_e should be always guaranteed for vibration reduction and $2a$ should be always avoided. Thus, regular maintenance works are essential to avoid air entrainment in the working fluid and looseness of the damper fixings.

The nonlinear physical in-service damper model and the vehicle dynamic response characteristics obtained in this research could be used in product design optimisation and optimal specification of high-speed rail hydraulic dampers.

Acknowledgement

The authors thank financial supports from the National Natural Science Foundation of China (NSFC) under Grant No. 11572123 and the State Key Laboratory for Strength and Vibration of Mechanical Structures of China under Project No. SV2016-KF-05.

References

[1] A.C. Mellado, E. Gómez, J. Viñolas, Advances on railway yaw damper characterisation exposed to small displacements, Int. J. Heavy Veh. Syst. 13 (4) (2006) 263–280.

[2] W.L. Wang, Y. Huang, X.J. Yang, G.X. Xu, Nonlinear parametric modeling of a high-speed rail hydraulic yaw damper with series clearance and stiffness, Nonlinear Dyn. 65 (1–2) (2011) 13–34.

[3] W.L. Wang, D.S. Yu, Y. Huang, Z. Zhou, R. Xu, A locomotive's dynamic response to in-service parameter variations of its hydraulic yaw damper, Nonlinear Dyn. 77 (4) (2014) 1485–1502.

[4] R.V. Kasteel, C.G. Wang, L.X. Qian, J.Z. Liu, G.H. Ye, A new shock absorber model for use in vehicle dynamics studies, Veh. Syst. Dyn. 43 (9) (2005) 613–631.

[5] A. Farjoud, M. Ahmadian, M. Craft, W. Burke, Nonlinear modeling and experimental characterization of hydraulic dampers: effects of shim stack and orifice parameters on damper performance, Nonlinear Dyn. 67 (2) (2012) 1437–1456.

[6] A. Simms, D. Crolla, The influence of damper properties on vehicle dynamic behavior, SAE Paper, 2002–01–0319.

[7] J.A. Calvo, B. López-Boada, J.L.S. Román, A. Gauchía, Influence of a shock absorber model on vehicle dynamic simulation,

Proc. Inst. Mech. Eng. Part D: J. Automob. Eng. 223 (2) (2009) 189–202.

[8] C.K. Park, Y.G. Kim, D.S. Bae, Sensitivity analysis of suspension characteristics for Korean high speed train, J. Mech. Sci. Tech. 23 (2009) 938–941.

[9] N.C. Shieh, C.L. Lin, Y.C. Lin, K.Z. Liang, Optimal design for passive suspension of a light rail vehicle using constrained multiobjective evolutionary search, J. Sound Vib. 285(1–2) (2005) 407–424.

[10] Y.P. He, J. Mcphee, Multidisciplinary optimization of multibody systems with application to the design of rail vehicles, Multibody Syst. Dyn. 14 (2005) 111–135.

[11] J.H. Hao, J. Zeng, P.B. Wu, Vertical stochastic vibration reduction and suspension parameters optimization of a railway passenger car, J. China Railway Society 28(6) (2006) 35–40. (In Chinese)

[12] European Standard: Railway Applications – Suspension Components – Hydraulic Dampers, EN 13802:2013.

[13] W.L. Wang, D.S. Yu, Z. Zhou, In-service parametric modelling a rail vehicle's axle-box hydraulic damper for high-speed transit problems, Mech. Syst. Signal Process. 62–63 (2015) 517–533.

[14] W.L. Wang, D.S. Yu, S. Iwnicki, Nonlinear optimal specification of a locomotive axle-box hydraulic damper for vibration reduction and track-friendliness, Proceedings of the 24th Symposium of the International Association for Vehicle System Dynamics, pp. 1471-1480, August 17-21, 2015, Graz, Austria.

[15] A.P. Boresi, K.P. Chong, J.D. Lee, Elasticity in Engineering Mechanics (3rd edition), John Wiley & Sons, INC., Hoboken, New Jersey, USA, 2011.

[16] C.C. Zhou, Theory and Design of Automotive Shock Absorber, Beijing University Press, Beijing, China, 2012. (In Chinese)

[17] M.G. Rabie, Fluid Power Engineering. The McGraw-Hill Companies, Inc., New York, USA, 2009.

[18] J.C. Dixon, The Shock Absorber Handbook, John Wiley & Sons, Ltd., West Sussex, England, 2007.

[19] Chinese Railway Society Standard, Evaluation methods and criteria for dynamics performance test of railway locomotives, TB/T 2360-93, 1993. (In Chinese)

[20] S. Iwnicki, Handbook of Railway Vehicle Dynamics, Taylor & Francis Group, Abingdon, England, 2006.